Hierarchical Abstraction of Compensator for Reaction Torque Observer Based on Element Description Method

Issei Takeuchi 🅾, *Member, IEEE*, and Seiichiro Katsura 🅾, *Member, IEEE*

Abstract—The expansion of the applicable range of robots and machines requires the ability to cooperate with humans and adapt to external environments. It is necessary to use torque information in order to achieve these capabilities. A reaction torque observer is one of the effective methods to obtain torque information because it does not need a torque sensor and it can deal with torque information in the high-frequency domain. However, it needs a correct compensator to reject disturbances to estimate the precise torque. Generally, the disturbance compensator of the reaction torque observer is derived by manual model selection and manual/automatic parameter fitting. This method not only takes time and effort but also does not always obtain an optimal solution because it depends on a predetermined model. In particular, it is well known that nonlinear elements such as friction are difficult to model. To overcome this issue, an automatic design method of a disturbance compensator is proposed in this article. The compensator is abstracted automatically using an element description method. Using the element description method, model design in advance is not needed because the model selection and the parameter fitting are conducted simultaneously. Therefore, the element description method can be applied to systems whose model structure is unknown. In addition, it is possible to input human intentions as initial settings. These features enable designs that make use of human knowledge and the computational power of computers.

Index Terms—Friction identification, genetic algorithm, reaction torque observer, system abstraction.

I. INTRODUCTION

IN RECENT years, the activity range of human and robot has become closer in daily life because of the declining labor population due to the declining birthrate and increasing aging population [1], [2]. It is a well-known fact that torque control technology is important to achieve the cooperation between humans and robots [3], [4]. Consequently, the importance of reaction torque analysis and control technology for industrial machinery has been increasing. For a more precise reaction torque control, wide-band and high-accuracy torque sensing technology is indispensable. A reaction torque observer (RTOB) [5] is one of the effective methods in order to acquire reaction torque information. The RTOB is able to deal with high-frequency-domain torque information and does not require the addition of a torque sensor. Hence, several advantages in the torque control system can be obtained by using the RTOB such as achieving higher bandwidth, stability improvement, and cost reduction [6], [7]. Moreover, since it can be configured into a variable structure, adaptive calculation of the RTOB can be achieved [8]. Currently, the RTOB is used in industrial machinery [9]. However, in order to acquire the correct torque information by the RTOB, a precise and strict compensator is needed. An environmental quarrier [10] can remove disturbances such as friction torque and acquire highly accurate reaction torque information without deriving a mathematical model. However, the cost increases because a pair of drive systems having the same structure are required. A high-precision reaction force observer using a notch filter [11] has been proposed. This method can reduce the influence of friction torque by adding a dither signal. However, the dither signal can adversely affect the intended task. In this article, model-based disturbance compensation methods are focused.

Generally, the disturbance compensator of the RTOB is derived by manual model selection and parameter fitting. This method not only demands extensive time and effort but is also not always optimal because it depends on the predetermined model known by the engineer. Particularly, nonlinear functions such as friction [12], [13] are difficult to identify. A LuGre-model-based friction-compensation method [14], [15] is known to be effective to compensate friction influence. This method can consider several influences such as the Sribeck effect, hysteresis, and stick-slip limit cycling. However, its implementation demands also extensive time and effort as the structure is slightly complicated. On the other hand, compensation methods of disturbance using machine learning such as neural networks (NN) have been proposed [16]–[19]. Since these methods do not need a predetermined model in the NN parts, a more optimal solution is derived. However, the physical meaning of the identification results in the NN is hard to understand because the compensator is expressed by the weight of each node.

To overcome these problems, this article proposes an automatic design method of a disturbance compensator. The

Issei Takeuchi is with the Advanced Technology Research Division, Tokyo Automatic Machinery Works, Ltd., Tokyo 101-0032, Japan (e-mail: issei@tam-tokyo.co.jp).

Seiichiro Katsura is with the Department of System Design Engineering, Keio University, Yokohama 223-8522, Japan (e-mail: katsura@sd.keio.ac.jp).

Fig. 1.   Element matrix used for the EDM.

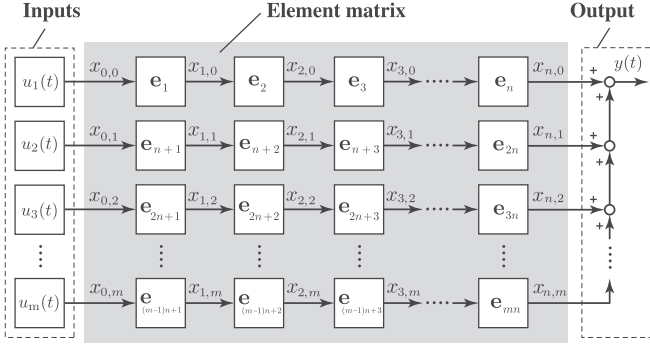Fig. 2.   DNA structure for the EDM.

Fig. 3.   Basic elements. (a) Through. (b) Invert. (c) Offset.

compensator is generated automatically using an element description method (EDM) [20]. By using the EDM, a model designed in advance is not needed because the model selection and the parameter fitting are conducted simultaneously. Therefore, it is possible to abstract unknown systems by the EDM. Moreover, the EDM can deal with nonlinear functions easily. When the EDM is used hierarchically, since it is possible to extract relevant physical equations in order of importance, the target system is abstracted as necessary, thus obtaining sufficient accuracy. In addition, the abstraction result of the EDM can succeed to the next abstraction. Therefore, increasingly better results can be derived when subjecting the abstraction to more repetitions with different situations. Hence, the proposed method can be expected to be applied to Industrial IoT [21] and Industry 4.0 [22] as a machine learning technology that enables humans to understand the meaning of the learning results of the model and inherits it to the next generation as knowledge. Using the proposed method, the implementation of the compensator for the RTOB becomes easier.

The rest of this article is organized as follows. In Section II, the EDM is introduced. In Section III, an abstraction method of the disturbance compensator by the EDM is proposed. In Section IV, validity of the proposed method is confirmed by experiments using an actual industrial application. Finally, Section V concludes the article.

II. ELEMENT DESCRIPTION METHOD

In this section, the concept of the EDM is explained. In the EDM, a system is expressed by an element matrix defined as a combination of simple elements. Fig. 1 shows the element matrix. In Fig. 1, x denotes the signal flow of horizontal direction. The center area in Fig. 1 stands for the element matrix. $n \in \mathbb{N}$ and $m \in \mathbb{N}$ denote the row size and the column size of the element matrix, respectively. The matrix size can be decided arbitrarily according to the purpose. $u_\bullet(t)$ and $y(t)$ stand for the input signals for the system and the output signal from the system, respectively. The calculation is conducted sequentially from the left top to the right bottom, using the input signal. The calculation of j-row and i-column element is expressed by

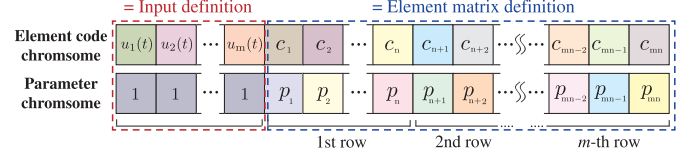$$x_{i+1,j} = f_\alpha(x_{i,j}), \quad (\alpha = jn + i + 1) \tag{1}$$
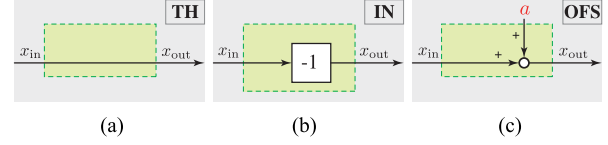
where f_α stands for the calculation function. $\alpha \in \mathbb{N}$ denotes the address of each element. Each element is expressed as a single-input and single-output system. The output value of each element is used for the adjacent element as input value.

In the EDM, the element matrix is optimized by genetic algorithms (GAs) [23]–[26]. Fig. 2 stands for chromosome structure used for the EDM. There are two chromosomes; one is the element code chromosome, the other is the parameter chromosome. The element code chromosome and the parameter chromosome are designed to be paired. The calculation of each element is conducted based on the chromosome vector $\mathbf{g}_\beta$ expressed as

$$\mathbf{g}_\beta = \begin{cases} \mathbf{u}_\beta = \{u_\beta, 1\}^{\mathrm{T}} [1 \leq \beta \leq m] \\ \mathbf{e}_\alpha = \{c_\alpha, p_\alpha\}^{T} [m < \beta \leq (n+1)m] \end{cases} \quad \because \alpha = \beta - \mathrm{m} \tag{2}$$

where $\beta \in \mathbb{N}$, $u_\bullet$, $c_\bullet$, and $p_\bullet$ refer to the address of chromosome, the input code, the element code, and element parameter, respectively. In the case of $1 \leq \beta \leq m$, the element code chromosomes u_β express kind of input values. One of the input values prepared by the designer in advance is automatically selected according to u_β. Since the parameter is not required in the case of $1 \leq \beta \leq m$, the parameter chromosomes are fixed at 1. In the case of $m < \beta \leq (n+1)m$, c_α and p_α express the kind of elements of f_α and the parameter in f_α, respectively. The type of selectable element can be arbitrarily determined according to the objective. Examples of the elements are shown in Figs. 3–5. x_{in} and x_{out} stand for the input value and the output value of the element, respectively. Fig. 3 depicts the basic elements to construct the element matrix structure. Fig. 4 expresses the calculation elements. Fig. 5 stands for the nonlinear function elements. For simplification, Fig. 4 represents the transfer function in the frequency domain using the Laplace operator s, but the calculation is actually performed in the time domain. $c_\bullet$ is a variable that specifies the code shown in the upper right of each element in Figs. 3–5, and $p_\bullet$ is the value of the parameter a in each element in Figs. 3–5. The parameter of each element is limited within the arbitrary range. The elements shown in this figure are merely examples. Various elements can be prepared according to necessity. For example, an element of first-order low-pass filter ($c_\alpha = \mathbf{LPF}$) is calculated as follows:

$$x_{\mathrm{out}}(s) = \frac{a_{\mathrm{lpf}}}{s + a_{\mathrm{lpf}}} x_{\mathrm{in}}(s) \tag{3}$$
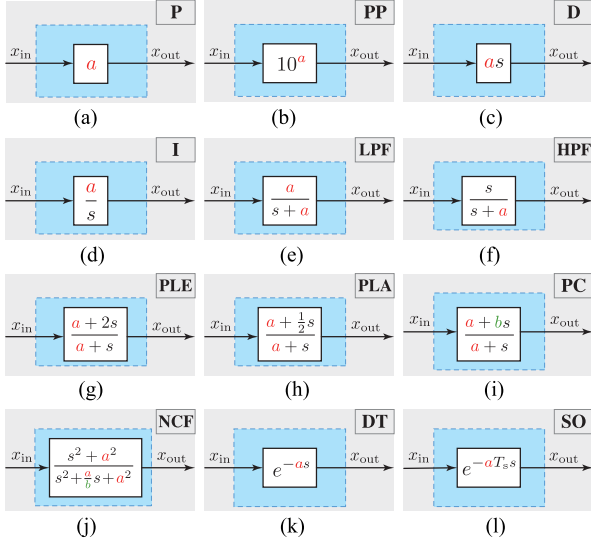
Fig. 4. Calculation elements. (a) Gain. (b) Power gain. (c) Derivation. (d) Integral. (e) Low-pass filter (f) High-pass filter. (g) Phase-lead compensator. (h) Phase-lag compensator. (i) Phase compensator. (j) Notch filter. (k) Dead time. (l) Shift operator.
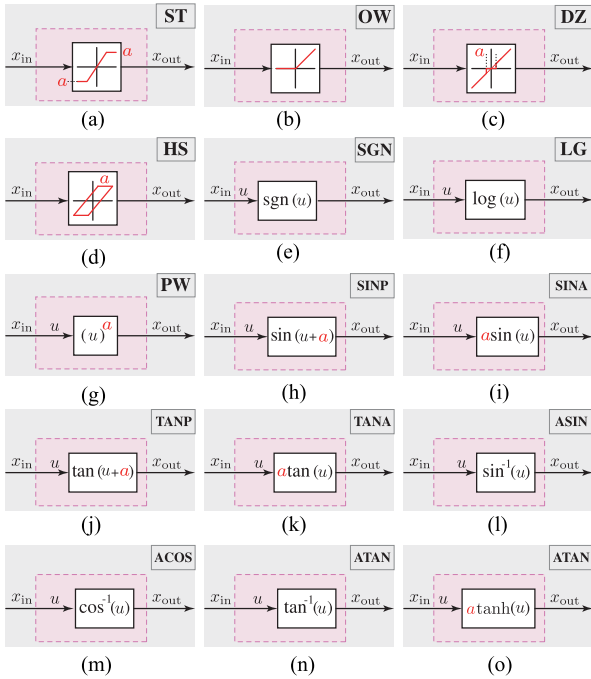

Fig. 5. Nonlinear function elements. (a) Satuation. (b) One way. (c) Dead zone. (d) Hysteresis. (e) Sign function (f) Logarithmic function. (g) Power. (h) Sine wave (phase). (i) Sine wave (amp.). (j) Tangent (phase). (k) Tangent (amp.). (l) Arc sine. (m) Arc cosine. (n) Arc tangent. (o) Hyperbolic tangent.

where a_{lpf} denotes the cutoff frequency of the low-pass filter. a_{lpf} is calculated by

$$a_{\mathrm{lpf}} = (p_{\mathrm{lpf}}^{\max} - p_{\mathrm{lpf}}^{\min}) p_\alpha + p_{\mathrm{lpf}}^{\min} \qquad (4)$$

where $p_{\mathrm{lpf}}^{\max}$, $p_{\mathrm{lpf}}^{\min}$, and p_α refer to the maximum value and the minimum value used for the low-pass filter element, and a random value ranged by 0 to 1, respectively. $p_{\mathrm{lpf}}^{\max}$ and $p_{\mathrm{lpf}}^{\min}$ can be designed arbitrarily according to the kind of elements. Moreover,
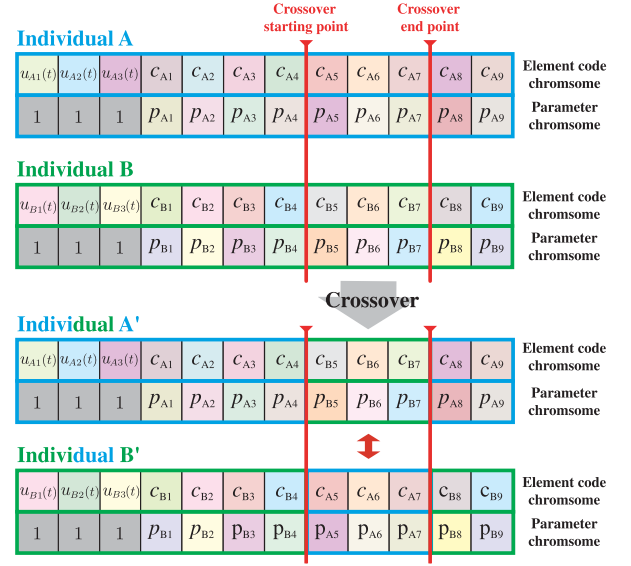

Fig. 6. Overview of the crossover process.

when the element affects the calculation logarithmically, a_{lpf} is set logarithmically by

$$a_{\mathrm{lpf}} = 10^{(p_{\mathrm{lpf}}^{\max} - p_{\mathrm{lpf}}^{\min}) p_\alpha + p_{\mathrm{lpf}}^{\min}}. \qquad (5)$$

For example, in the case of an element such as a low-pass filter, the upper and lower limits are the control band of the target system as follows:

$$\frac{2\pi}{T_{\mathrm{sum}}} \le a_{\mathrm{lpf}} \le \frac{\pi}{T_s} \qquad (6)$$

where T_{sum} and T_s stand for total time of time-series data and sampling time, respectively. The upper limit value represents the Nyquist frequency. In the case of the dead time element, the control period is the lower limit and the total time is the upper limit

$$T_s \le a_{\mathrm{dt}} \le T_{\mathrm{sum}} \qquad (7)$$

where a_{dt} denotes the dead time. Moreover, when aiming at a specific range, it is possible to set the range narrowly. The optimization procedure of the EDM is based on the general procedure of GA [20]. The evolutionary process consists of selection, crossover, parameter-shift, and mutation processes. In the selection process, individuals to be used in the next generation are selected. In the crossover process, whether to perform an intersection is determined probabilistically for every individual based on a crossover rate. The element code chromosomes and the parameter chromosomes of the individual that selected in the crossover process are exchanged together. The crossover process is depicted in Fig. 6. In the parameter-shift process, parameters selected probabilistically are slightly increased or decreased. In the mutation process, the chromosomes are stochastically rewritten based on the mutation rate. The parameter-shift process and the mutation process are shown in Fig. 7. The GA for the EDM is summarized in Algorithm 1. $G_{\max}$ and I_{num} denote number of generation changes and number of individuals, respectively. Generally, when GA is applied to motion control,
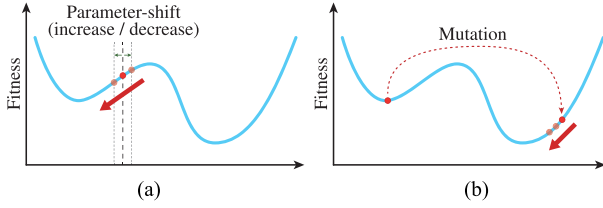
Fig. 7. Overviews of the parameter-shift and the mutation process. (a) Parameter-shift process. (b) Mutation process.

Algorithm 1: GA for the EDM.

Initialization ()
Data get ()
while age $\leq G_{\max} \times$ rep **do**
  for cntr = 1 to I_{num} **do**
    while $t < T_{\text{sum}}$ **do**
      Matrix calculation
      Fitness calculation
    end while
    F [cntr] = Fitness
  end for
  Ranking ()
  Selection ()
  Crossover ()
  Parameter shift()
  Mutation ()
  Make new age
  if $G_{\max} \times$ rep $\leq$ age **then**
    if continue = "Yes" **then**
      rep $\Leftarrow$ rep +1
    end if
  end if
end while

Fig. 8. Overview of the hierarchical abstraction.

Fig. 9. Block diagram of the RTOB.

only the parameters are optimized by predetermining the structure of the system [26]. Using the proposed method, not only the parameters but also the structure of the system and the selection of input parameters can be optimized at the same time. When the termination conditions are satisfied, the best individual is dealt as the abstraction result.

By analyzing the results of the EDM, the physical meaning is grasped. In addition, the results of the EDM can be used in the next optimization as the initial population. By using an elite preservation strategy, the result will not be deteriorated. In addition, by performing the optimization hierarchically, it is possible to extract the physical laws in order of importance for the system expression. The hierarchical abstraction is performed by increasing the size of the element matrix while inheriting the model obtained in the past. An overview of the hierarchical optimization is depicted in Fig. 8. The system is abstracted by terminating the optimization process when sufficient accuracy is obtained by the hierarchical optimization. On the one hand, when the abstraction depth is shallow, the system can be abstracted with a reasonable accuracy using a simple mathematical model. On the other hand, when the abstraction depth is
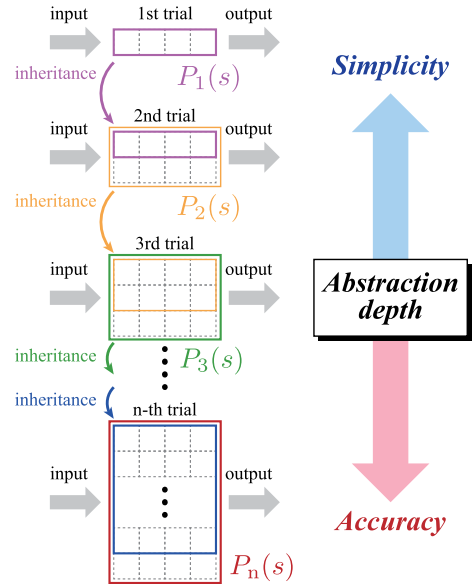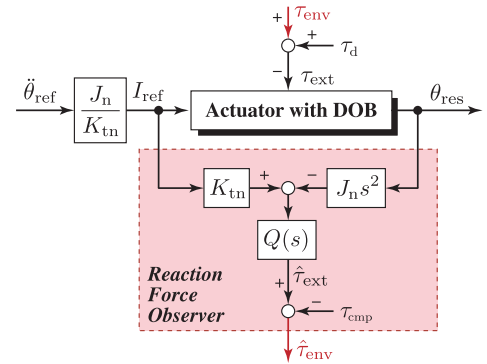
increased, the system can be abstracted with high precision using a more complicated mathematical model. The accuracy and simplicity are determined by the abstraction depth.

III. AUTOMATIC GENERATION OF THE COMPENSATOR FOR THE RTOB USING THE EDM

In this section, an automatic generation method of the compensator for the RTOB using the EDM is proposed. In this study, the RTOB for estimating the external torque applied to a servo motor is used for discussion as an example. The block diagram of the RTOB is expressed as Fig. 9. τ_{env}, τ_{ext}, τ_d, τ_{cmp}, I_{ref}, θ_{res}, J_n, and K_{tn} stand for the reaction torque from environment, external torque, disturbance torque, compensation torque, current reference value, angle response value, nominal value of inertia, and nominal value of torque constant, respectively. The superscript $\hat{\bullet}$ refers to the estimated value. $Q(s)$ expresses the low-pass filter of the RTOB. The actuator is moved by acceleration control with a disturbance observer (DOB) [27], [28]. The cutoff frequency of $Q(s)$ can be designed separately from the cutoff frequency of the DOB. To obtain pure reaction
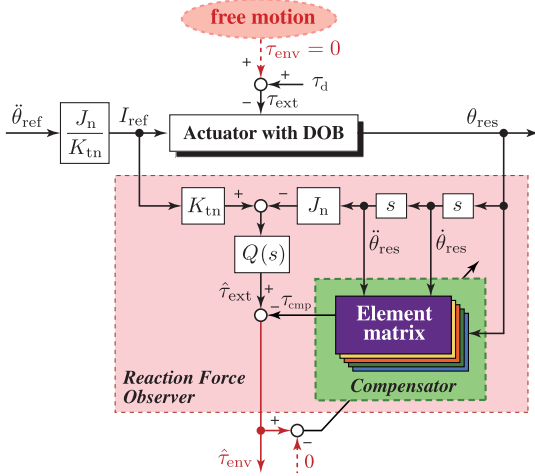
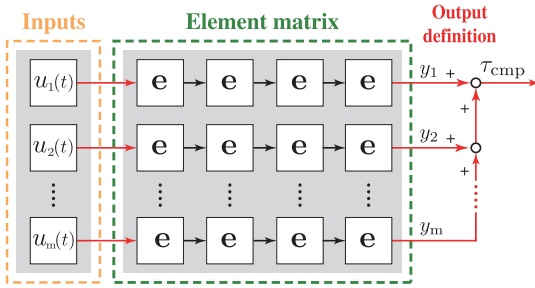Fig. 10.   Block diagram of the EDM for abstraction of the RTOB compensator.

Fig. 11.   Element matrix for abstraction of the RTOB compensator.

Fig. 12.   Experimental setup. (a) Structure of auger filling machine. (b) Picture of the auger part.

torque $\hat{\tau}_{\mathrm{ext}}$ from environments, it is necessary to compensate the disturbance torque τ_d. Therefore, the accurate calculation method of τ_d is needed to design the RTOB. Then, the estimated τ_d can be used as the compensation torque τ_{cmp}. Here, calculation methods of τ_{cmp} are introduced. Fig. 10 depicts a block diagram of automatic generation of the RTOB compensator by the EDM. The element matrix in Fig. 10 shows a compensator for the RTOB. The structure of the element matrix in Fig. 10 is expressed as Fig. 11. The input values can be set manually by arbitrary parameters or selected automatically by the EDM. In this study, the input values were selected automatically using the EDM. In this case, the inputs of the element matrix were designed as the status information of actuator. In addition, the sum of the outputs refers to a compensation torque for the RTOB. As the $\hat{\tau}_{\mathrm{ext}}$ contains the entire disturbance of the system, it is necessary to cancel the disturbances other than the reaction torque. The objective of generation of the compensator is to cancel these disturbances. The compensator is generated using free motion response of the actuator. At this time, it is desirable to move the motor so as to excite various disturbances.

When the RTOB works ideally, the torque response of the free motion become always zero. Therefore, the fitness function is defined as

$$\Gamma_{\mathrm{rtob}} = \sqrt{\frac{1}{N_{\mathrm{sum}}} \sum_{q=1}^{N_{\mathrm{sum}}} \Lambda(q) \cdot \hat{\tau}_{\mathrm{ext}}(q)^2} \qquad (8)$$

where q, Γ_{rtob}, N_{sum}, and $\Lambda(q)$ refer to sampling number, the fitness value, total number of time-series data of free motion, and the weighting function, respectively. The individuals with small fitness values are more likely to survive in the next generation. By repeating the evolution, an equation for calculating the compensation value for zeroing the estimated torque is automatically derived.

IV. Experiments

In this section, experiments were conducted to confirm the validity of the proposed method. The experiments consist of two phases, an abstraction phase and an evaluation phase. In the abstraction phase, the model of RTOB compensator is extracted using experimental data. In the evaluation phase, the RTOB compensator generated in the abstraction phase is applied to the new experimental data, and the compensation accuracy is evaluated. In the experiments, compensation accuracy of the conventional method and the proposed method were compared.

A. Experimental Setup

The experimental setup is shown in Fig. 12. This equipment is a powder-filling machine. The machine fills various powders by a screw shaft called auger. Fig. 12(b) depicts the auger part. The auger is actuated by a servo motor. In addition, the auger axis is supported by bearings to reduce the fluctuation. The bearings are sealed to avoid contamination of the powder into the actuator. Thereby, friction due to the sealed parts and the bearings exists. The characteristics of the friction are depicted in Fig. 13. In these experiments, the friction model of the auger-filling machine was abstracted for designing the RTOB.

Then, time-series data were prepared for abstraction of the compensator. The actuator is moved by angular velocity control. The angular velocity step command was applied from 0 to 10 s. In addition, angular velocity chirp command was given after
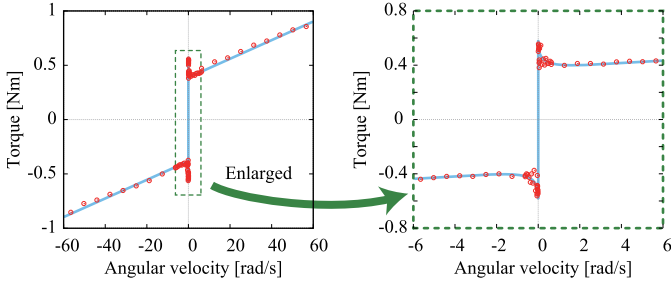
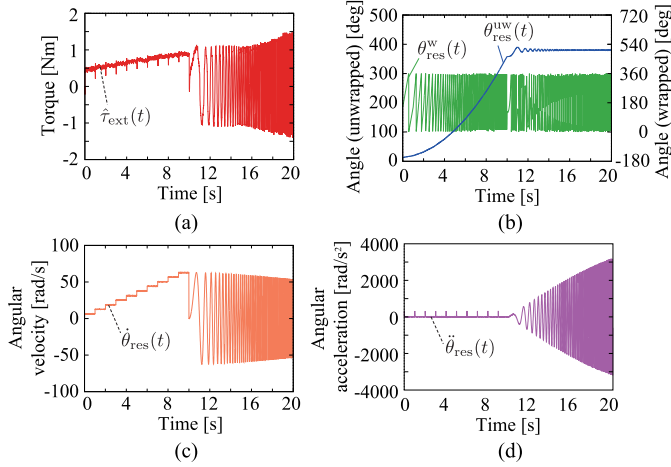Fig. 13. Friction characteristics of the auger axis.

Fig. 14. Time-series data for abstraction of the compensator. (a) Torque. (b) Angle (c) Angular velocity. (d) Angular acceleration.
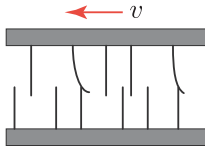

Fig. 15. LuGre model.

10 s. The chirp signal is designed as follows:

$$\omega_{\mathrm{cmd}} = 20\,\pi \sin\left\{2\pi \times 0.5(t - 10)^2\right\} \qquad (9)$$

where ω_{cmd} stands for the angular velocity command. Fig. 14 shows the prepared time-series data for abstraction. $\hat{\tau}_{\mathrm{ext}}(t)$, $\theta_{\mathrm{res}}^{\mathrm{w}}(t)$, $\theta_{\mathrm{res}}^{\mathrm{uw}}(t)$, $\dot{\theta}_{\mathrm{res}}(t)$, and $\ddot{\theta}_{\mathrm{res}}(t)$ stand for estimated external torque, wrapped angle response, unwrapped angle response, angular velocity response, and angular acceleration response, respectively. In this case, $\theta_{\mathrm{res}}^{\mathrm{w}}(t)$, $\theta_{\mathrm{res}}^{\mathrm{uw}}(t)$, and $\dot{\theta}_{\mathrm{res}}(t)$ are input values for abstraction, and $\hat{\tau}_{\mathrm{ext}}(t)$ means training data, respectively. These variables are the same as those depicted in Fig. 10.

B. Conventional Method

In this article, a friction compensator based on a LuGre model [14], [15] was applied as the conventional method. A conceptual diagram of the LuGre mode is shown in Fig. 15. The LuGre model is known as a rigid friction model. The frictional

TABLE I
IDENTIFICATION RESULTS OF THE LuGre MODEL

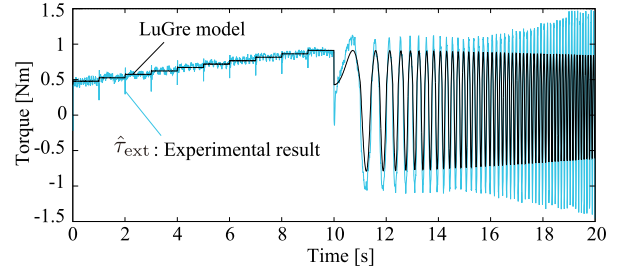| Parameter	Value
$\dot{\nu}_{\mathrm{s}}$	1.0001×10^{-8}
τ_{c}	0.98840
τ_{s}	7.0244×10^{-8}
z	3.8859×10^{-7}
σ_0	1.1048×10^{6}
σ_1	0.013570
σ_2	8.7536×10^{-8}

Fig. 16. Torque response of the LuGre model.

torque represented by the LuGre model is defined as

$$\tau_{\mathrm{fric}} = \sigma_0 z + \sigma_1 \frac{dz}{dt} + \sigma_2 \dot{\nu} \qquad (10)$$

where τ_{fric}, z, $\dot{\nu}$, σ_0, σ_1, and σ_2 stand for the friction torque, deflection of the bristles, relative velocity of moving part, bristle stiffness, bristle damping coefficient, and viscous damping coefficient, respectively. The motion equation about z is represented as

$$\frac{dz}{dt} = \dot{\nu} - \frac{|\dot{\nu}|}{g(\dot{\nu})} z \qquad (11)$$

where $g(\dot{\nu})$ is the function indicating the Stribeck effect and is expressed as follows:

$$g(\dot{\nu}) = \frac{\tau_{\mathrm{c}} + (\tau_{\mathrm{s}} - \tau_{\mathrm{c}}) e^{-(\dot{\nu}/\dot{\nu}_{\mathrm{s}})^2}}{\sigma_0} \qquad (12)$$

where τ_{c}, τ_{s}, and $\dot{\nu}_{\mathrm{s}}$ stand for Coulomb friction level, stiction torque, and Stribeck velocity, respectively. When $\dot{\nu}$ is constant, z is in steady state as

$$z_{\mathrm{ss}} = g(\dot{\nu})\,\mathrm{sgn}(\dot{\nu}). \qquad (13)$$

In addition, the relationship between the angular velocity and the frictional torque in the steady state is expressed as

$$\tau_{\mathrm{ss}}(\dot{\nu}) = \sigma_0 g(\dot{\nu})\,\mathrm{sgn}(\dot{\nu}) + \sigma_2 \dot{\nu}$$
$$= \tau_{\mathrm{c}}\,\mathrm{sgn}(\dot{\nu}) + (\tau_{\mathrm{s}} - \tau_{\mathrm{c}}) e^{-(\dot{\nu}/\dot{\nu}_{\mathrm{s}})^2}\,\mathrm{sgn}(\dot{\nu}) + \sigma_2 \dot{\nu}. \qquad (14)$$

In the experiments, the parameters of the LuGre model are calculated by GA. Equation (8) was used as a fitness function for the identification of the LuGre model. The derived parameters are shown in Table I. The torque response using the LuGre model is shown in Fig. 16.
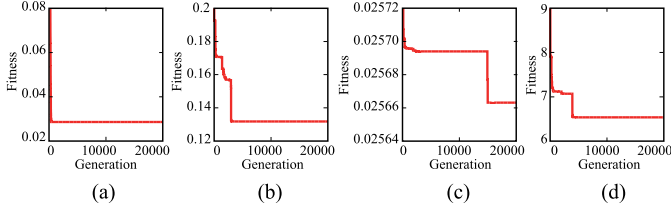
Fig. 17. Fitness responses in abstraction phase. (a) Step 1. (b) Step 2. (c) Step 3. (d) Step 4.

C. Abstraction of the RTOB Compensator Using the EDM.

The EDM was applied to abstract a disturbance compensator for the RTOB. The abstraction was conducted hierarchically as shown in Fig. 8. In this study, the hierarchical abstraction was performed in Steps 1–4.

1) Step 1: In Step 1, angular velocity-dependent characteristics were extracted using experimental data of constant velocity. Therefore, the weighting function was designed as follows:

$$\Lambda(q) = \begin{cases} 1 & (0 \le t < 10) \\ 0 & (10 \le t \le 20). \end{cases} \tag{15}$$

In Step 1, a 4×2 element matrix was prepared. In addition, a model of Coulomb friction/viscous friction was provided as an initial model. When an important model is known, the model can be given as an initial value for faster optimization. The fitness responses and the torque responses in abstraction phase are depicted in Figs. 17 and 18, respectively. The fitness response and the torque response in Step 1 are shown in Figs. 17(a) and 18(g). The results of the abstraction in Step 1 is shown in Fig. 19(a).

2) Step 2: When performing hierarchical abstraction, it is necessary to increase the number of rows at each step. Hence, a 4×3 element matrix was prepared in Step 2. In the hierarchical abstraction, the abstraction result of the previous step is inherited as the initial value of the next step. This concept of inheritance is shown in Fig. 19. In Fig. 19, rand () denotes a random value. From Fig. 18(g), it can be seen that the model of Step 1 cannot express the angular acceleration-dependent response after 10 s. Therefore, in order to extract the angular acceleration-dependent term, optimization was performed with $\Lambda(q) = 1$ at all times in Step 2. The fitness response and the torque response in Step 2 are shown in Figs. 17(b) and 18(h). The output of the row extracted in Step 2 is shown in Fig. 18(c), and it can be seen that the angular acceleration-dependent term after 10 s can be expressed. The results of the abstraction in Step 1 is shown in Fig. 19(c).

3) Step 3: In Step 3, a 4×4 element matrix was prepared. Similar to Step 2, in Step 3, the optimization was performed by inheriting the result of the previous step as shown in Fig. 19(d). The weighting function was designed as (15) in Step 3. The fitness response and the torque response in Step 3 are depicted in Figs. 17(c) and 18(i). To confirm the improvement by Step 3, Fig. 18(h) and (i) are enlarged in Fig 20(a). From the result, it was confirmed that the spatially dependent high frequency was expressed in Step 3.
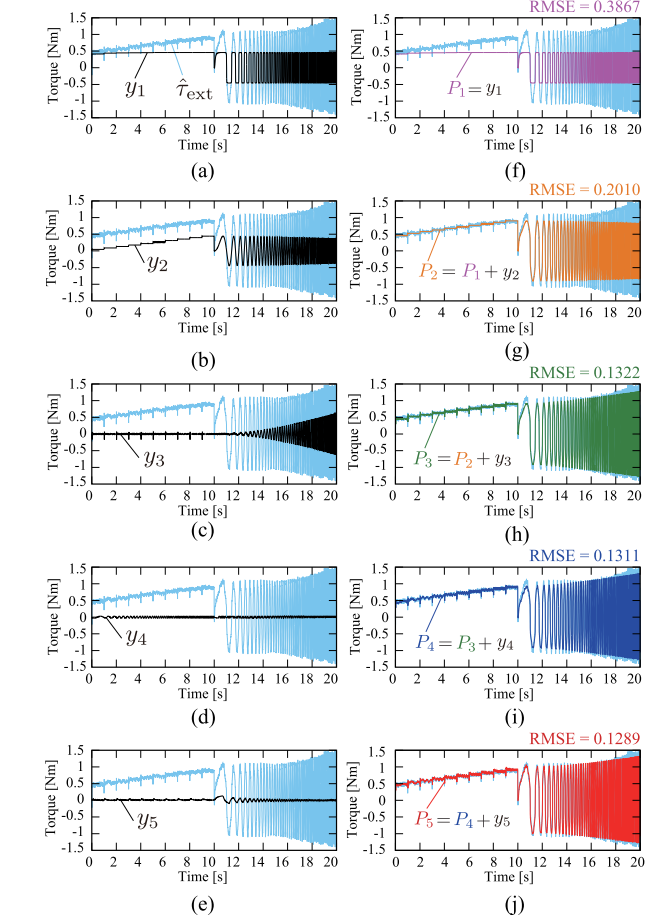

Fig. 18. Torque responses in abstraction phase. (a) Output from the 1st line. (b) Output from the 2nd line. (c) Output from the 3rd line. (d) Output from the 4th line. (e) Output from the 5th line. (f) Output from $P_1(s)$. (g) Output from $P_2(s)$. (h) Output from $P_3(s)$. (i) Output from $P_4(s)$. (j) Output from $P_5(s)$.
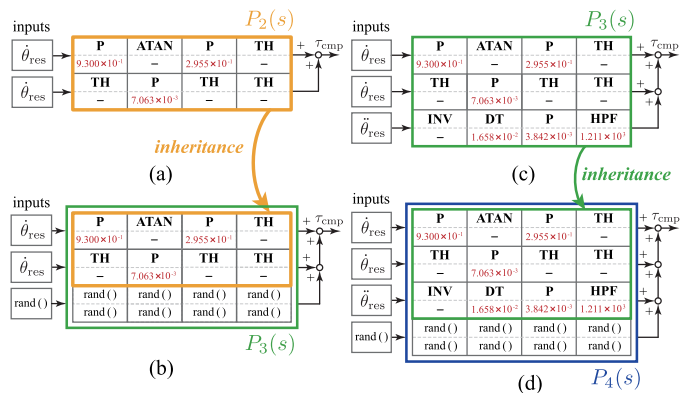

Fig. 19. Conceptual view of the inheritance. (a) Results of Step 1. (b) Initial settings for Step 2. (c) Results of Step 2. (d) Initial settings for Step 3.

4) Step 4: Similar to Step 3, the result of the previous step was inherited and a 4×5 matrix was prepared for optimization in Step 4. In view of the lack of gain in the frequency response after 10 s, the weighting function was designed in Step 4 as
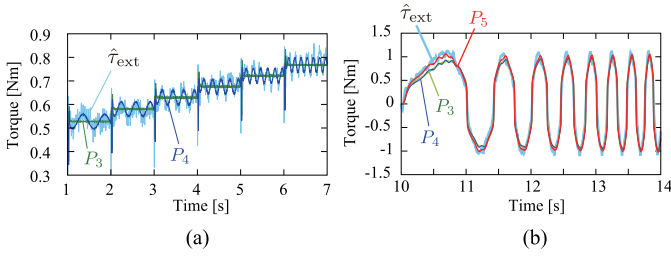
Fig. 20. Partial enlarged view of Fig. 18. (a) Comparison between Steps 2 and 3. (b) Comparison between Steps 2, 3, and 4.
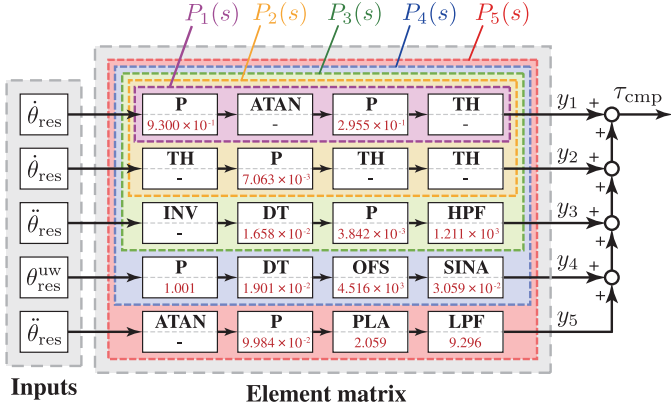

Fig. 21. Abstraction results by the EDM.

Fig. 22. Abstracted compensator by the EDM.

TABLE II
PARAMETERS IN FIG. 22

Parameter	Value
a_1	9.300×10^{-1}
a_3	2.955×10^{-1}
a_6	7.063×10^{-3}
a_{10}	1.658×10^{-2}
a_{11}	3.842×10^{-3}
a_{12}	1.211×10^{3}
a_{13}	1.001
a_{14}	1.901×10^{-2}
a_{15}	4.516×10^{3}
a_{16}	3.059×10^{-2}
a_{18}	9.984×10^{-2}
a_{19}	2.059
a_{20}	9.296

follows:

$$\Lambda(q) = \begin{cases} 20000 & (0.8 \le |\hat{\tau}_{\text{ext}}|) \\ 1 & (\text{otherwise}). \end{cases} \quad (16)$$

The fitness response and the torque response in Step 4 are depicted in Figs. 17(d) and 18(j). To confirm the improvement by Step 4, Figs. 18(h), (i), and (j) are enlarged in Fig. 20(b). From the result, it was confirmed that the gain in the frequency response after 10 s was improved in Step 4. As described above, in the model generation by the EDM, it is possible to give the engineer's design intention by the initial individual and the fitness function. Fig. 18(a)–(e) depict the compensation torque output by each row ($y_1 - y_5$). The final abstraction result is shown in Fig. 21. The upper part of each element depicts the code shown in Figs. 3–5, and the lower part of each element expresses the parameters. By decoding Fig. 21, the block diagram of the compensator is derived. The block diagram of the abstracted compensator by the EDM is shown in Fig. 22. The parameters from a_1 to a_{20} in elements are shown in Table II. In Fig. 22, the first and second rows show the term of Coulomb friction and viscous friction, respectively; the third and fifth rows express the angular acceleration-dependent term; the fourth row stands for spatially dependent friction. The root means square error (RMSE) of each row is shown in the upper right part of Fig. 18(f)–(j). It can be seen that the RMSE decreases as the number of rows increases. On the contrary, as the number of rows increases, the complexity of the model increases. Moreover, if the number of rows is increased too much, the state of overlearning occurs, and even if a good result is shown for the
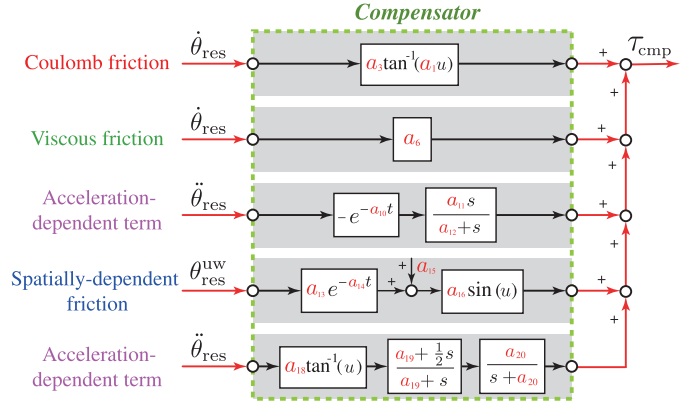
learning data, the result may be bad for the new data. Therefore, it is important for the engineer to interpret the physical meaning of the derived model and judge the model validity. The above is one of the excellent features of EDM because it cannot be done by NN in which the model becomes a black box.

D. Evaluation of Abstraction Result

To confirm the validity of the abstraction result by the EDM, torque responses using another time-series data from the abstraction phase were compared. The command angular velocity was designed as

$$\omega_{\text{cmd}} = 20 \pi \sin(2\pi \times 0.1 t^2). \quad (17)$$

The signal flow in the element matrix of the EDM is shown in Fig. 23. The rightmost waves in Fig. 23 show the output response of each row. In these figures, the scale of the vertical axis is unified, and it can be confirmed that the models in the first and second rows are important. On the contrary, the contribution of the third row, which had a high contribution in the abstraction phase, decreased in the evaluation phase. In addition, the contribution of the fifth row has increased. The reason is considered that the third row is a term that contributes to the compensation of high frequencies, and the operating frequency of the time-series data in the evaluation phase is lower than that in the abstraction phase. The comparison of the torque response is shown in Fig. 24. The enlarged view of Fig. 24 is depicted in
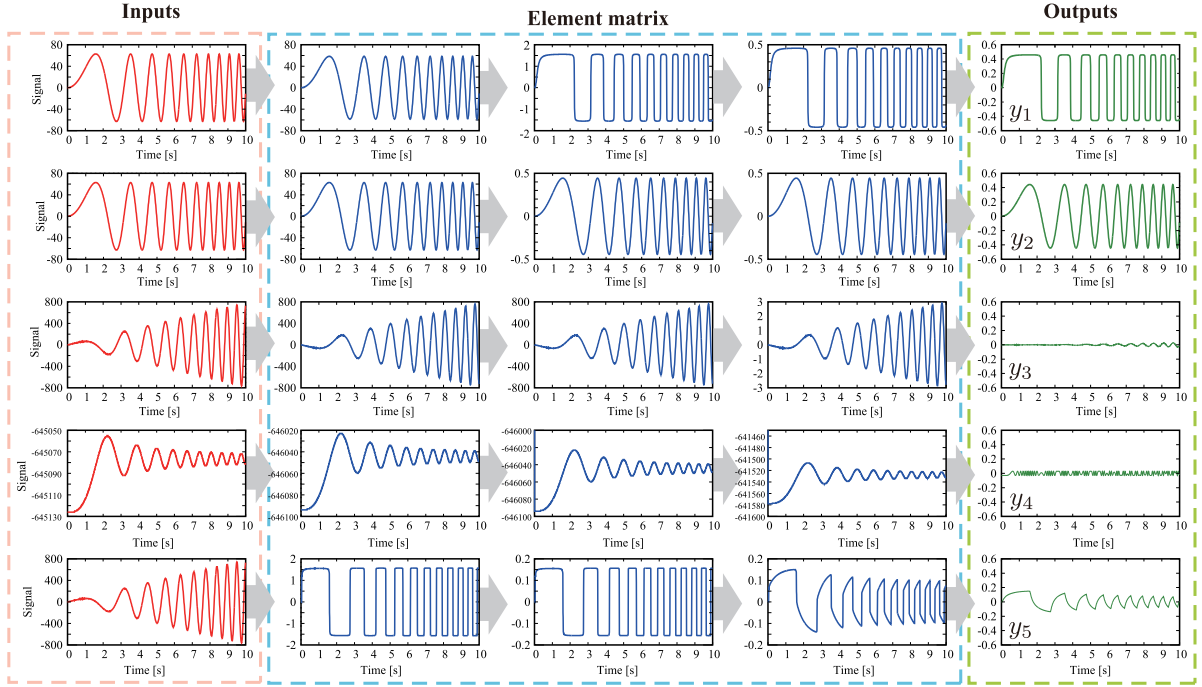
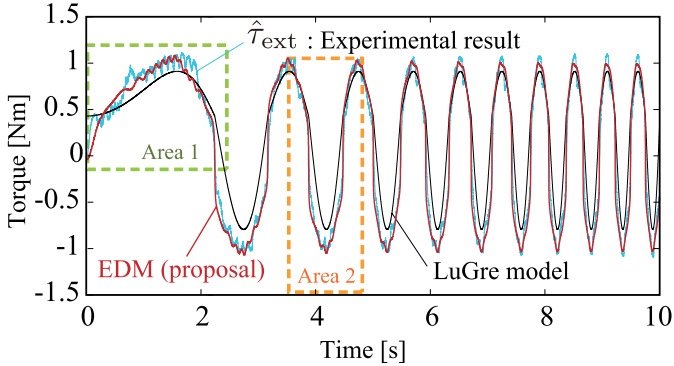Fig. 23.   Signal flow of the EDM in the evaluation phase.

Fig. 24.   Comparison of the torque responses between a conventional method and the proposed method in the evaluation phase.

TABLE III
COMPARISON OF THE RMSE IN THE EVALUATION PHASE

Method	RMSE	Unit
LuGre (conv.)	0.2798	Nm
EDM (prop.)	0.1254	Nm

Fig. 25.   Enlarged view of Fig. 24.

Fig. 25. It was confirmed that the proposed method can represent a few spatially dependent high frequencies, which could not be represented by conventional methods. This is the effect of the model on the fourth row. Moreover, the gain of the frequency response is closer to the experimental data in the proposed method than in the conventional method. This is the effect of the model on the fifth row. The comparison of the RMSE of the torque is shown in Table III. The RMSE of the proposed method is smaller than the conventional method. Therefore, the validity of the proposed method was confirmed by the experiments.
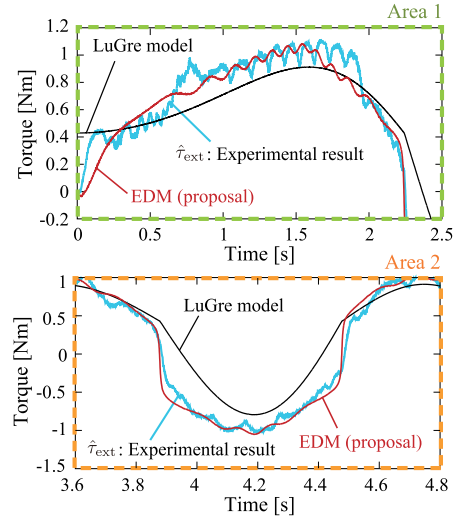
V. CONCLUSION

This article proposes the hierarchical abstraction method of a compensator for the RTOB using the EDM. Using the proposed method, compensator model and parameters can be simultaneously abstracted. Therefore, determining the disturbance model in advance is not needed when the compensator for the RTOB is designed. In addition, the hierarchical abstraction method can extract important physical laws in order of importance. The accuracy of the model is determined based on the abstraction depth by using the hierarchical abstraction procedure. As there is a tradeoff between simplicity and accuracy of the abstraction result, it is necessary to decide the abstraction depth based

on an accuracy requirement for the target application. Hence, using the proposed method, the model is abstracted with the necessary and sufficient model. In addition, the abstraction result is understandable because it is expressed by a combination of the simple elements. Although the proposed EDM may fall into overlearning like the NN, the possibility of falling into overlearning is less than that of NN because the validity of the abstracted model can be judged by interpreting the meaning of the model. Moreover, abstracted results can be inherited to different systems, so that this knowledge can be utilized. The EDM can be expected to develop as a machine learning method highly cooperative with humans.

REFERENCES

[1] K. Zinchenko, C. Y. Wu, and K. T. Song, "A study on speech recognition control for a surgical robot," *IEEE Trans. Ind. Informat.*, vol. 13, no. 2, pp. 607–615, Apr. 2017.

[2] E. Dean-Leon, K. Ramirez-Amaro, F. Bergner, I. Dianov, and G. Cheng, "Integration of robotic technologies for rapidly deployable robots," *IEEE Trans. Ind. Informat.*, vol. 14, no. 4, pp. 1691–1700, Apr. 2018.

[3] L. Roveda, G. Pallucca, N. Pedrocchi, F. Braghin, and L. M. Tosatti, "Iterative learning procedure with reinforcement for high-accuracy force tracking in robotized tasks," *IEEE Trans. Ind. Informat.*, vol. 14, no. 4, pp. 1753–1763, Apr. 2018.

[4] Q. Xu, "Design and smooth position/force switching control of a miniature gripper for automated microhandling," *IEEE Trans. Ind. Informat.*, vol. 10, no. 2, pp. 1023–1032, May 2014.

[5] T. Murakami, F. Yu, and K. Ohnishi, "Torque sensorless control in multi-degree-of-freedom manipulator," *IEEE Trans. Ind. Electron.*, vol. 40, no. 2, pp. 259–265, Apr. 1993.

[6] S. Katsura, Y. Matsumoto, and K. Ohnishi, "Modeling of force sensing and validation of disturbance observer for force control," *IEEE Trans. Ind. Electron.*, vol. 54, no. 1, pp. 530–538, Feb. 2007.

[7] Y. Park, N. Paine, and S. Oh, "Development of force observer in series elastic actuator for dynamic control," *IEEE Trans. Ind. Electron.*, vol. 65, no. 3, pp. 2398–2407, Mar. 2018.

[8] E. Sariyildiz and K. Ohnishi, "An adaptive reaction force observer design," *IEEE/ASME Trans. Mechatronics*, vol. 20, no. 2, pp. 750–760, Apr. 2015.

[9] Y. Ohba *et al.*, "Sensorless force control for injection molding machine using reaction torque observer considering torsion phenomenon," *IEEE Trans. Ind. Electron.*, vol. 56, no. 8, pp. 2955–2960, Aug. 2009.

[10] S. Katsura, K. Ohnishi, and K. Ohishi, "Transmission of force sensation by environment quarrier based on multilateral control," *IEEE Trans. Ind. Electron.*, vol. 54, no. 2, pp. 898–906, Apr. 2007.

[11] N. Kamiya, K. Ohishi, Y. Yokokura, and T. Miyazaki, "Force sensorless force control using notch-type dual disturbance observer," in *Proc. IEEE Int. Conf. Mechatronics*, Mar. 2019, pp. 504–509.

[12] Y. Maeda, K. Harata, and M. Iwasaki, "A friction model-based frequency response analysis for frictional servo systems," *IEEE Trans. Ind. Informat.*, vol. 14, no. 11, pp. 5146–5155, Nov. 2018.

[13] Z. Chen, B. Yao, and Q. Wang, "Adaptive robust precision motion control of linear motors with integrated compensation of nonlinearities and bearing flexible modes," *IEEE Trans. Ind. Informat.*, vol. 9, no. 2, pp. 965–973, May 2013.

[14] C. C. Wit, H. Olsson, K. J. Astrom, and P. Lischinsky, "A new model for control of systems with friction," *IEEE Trans. Automat. Control*, vol. 40, no. 3, pp. 419–425, Mar. 1995.

[15] L. Freidovich, A. Robertsson, A. Shiriaev, and R. Johansson, "LuGre-model-based friction compensation," *IEEE Trans. Control Syst. Technol.*, vol. 18, no. 1, pp. 194–200, Jan. 2010.

[16] S. Huang and K. K. Tan, "Intelligent friction modeling and compensation using neural network approximations," *IEEE Trans. Ind. Electron.*, vol. 59, no. 8, pp. 3342–3349, Aug. 2012.

[17] D. Xia, T. Chai, and L. Wang, "Fuzzy neural-network friction compensation-based singularity avoidance energy swing-up to nonequilibrium unstable position control of pendubot," *IEEE Trans. Control Syst. Technol.*, vol. 22, no. 2, pp. 690–705, Mar. 2014.

[18] Y. P. Kondratenko, O. V. Kozlov, O. S. Gerasin, and Y. M. Zaporozhets, "Synthesis and research of neuro-fuzzy observer of clamping force for mobile robot automatic control system," in *Proc. IEEE Int. Conf. Data Stream Mining Process.*, Lviv, Ukraine, Aug. 2016, pp. 90–95.

[19] Z. Wang, C. Hu, Y. Zhu, S. He, K. Yang, and M. Zhang, "Neural network learning adaptive robust control of an industrial linear motor-driven stage with disturbance rejection ability," *IEEE Trans. Ind. Informat.*, vol. 13, no. 5, pp. 2172–2183, Oct. 2017.

[20] I. Takeuchi and S. Katsura, "Model generation and parameter identification of unknown environment using element description method," in *Proc. IEEE Int. Conf. Mechatronics*, Feb. 2017, pp. 330–335.

[21] D. Zurita, M. Delgado, J. A. Carino, and J. A. Ortegan, "Multimodal forecasting methodology applied to industrial process monitoring," *IEEE Trans. Ind. Informat.*, vol. 14, no. 2, pp. 494–503, Feb. 2018.

[22] M. Indri, A. Grau, and M. Ruderman, "Guest editorial special section on recent trends and developments in Industry 4.0 motivated robotic solutions," *IEEE Trans. Ind. Informat.*, vol. 14, no. 4, pp. 1677–1680, Apr. 2018.

[23] K. S. Tang, K. F. Man, S. Kwong, and Q. He, "Genetic algorithms and their applications," *IEEE Signal Process. Mag.*, vol. 13, no. 6, pp. 22–37, Nov. 1996.

[24] S. B. Sulistyo, W. L. Woo, and S. S. Dlay, "Regularized neural networks fusion and genetic algorithm based on-field nitrogen status estimation of wheat plants," *IEEE Trans. Ind. Informat.*, vol. 13, no. 1, pp. 1103–114, Feb. 2017.

[25] F. Pistolesi, B. Lazzerini, M. D. Mura, and G. Dini, "EMOGA: A hybrid genetic algorithm with extremal optimization core for multiobjective disassembly line balancing," *IEEE Trans. Ind. Informat.*, vol. 14, no. 3, pp. 1089–1098, Mar. 2018.

[26] K. Itoh, M. Iwasaki, and N. Matsui, "Optimal design of robust vibration suppression controller using genetic algorithms," *IEEE Trans. Ind. Electron.*, vol. 51, no. 5, pp. 947–953, Oct. 2004.

[27] K. Ohishi, K. Ohnishi, and K. Miyachi, "Torque - speed regulation of DC motor based on load torque estimation method," in *Proc. IEEJ IPEC*, Mar. 1983, pp. 1209–1218.

[28] K. Ohnishi, M. Shibata, and T. Murakami, "Motion control for advanced mechatronics," *IEEE/ASME Trans. Mechatron.*, vol. 1, no. 1, pp. 56–67, Mar. 1996.

Issei Takeuchi (Member, IEEE) received the B.E. degree in electronic and communication engineering from Chuo University, Tokyo, Japan, in 2005, and the Ph.D. degree in integrated design engineering from Keio University, Yokohama, Japan, in 2018.

Since 2005, he has worked with the Department of Research and Development, the Advanced Technology Research Division, Tokyo Automatic Machinery Works, Ltd., Japan. His current research interests include motion control, artificial intelligence, and applied abstraction.

Dr. Takeuchi is a member of the Institute of Electrical Engineers of Japan (IEEJ) as well as a member of the Japan Society for Precision Engineering (JSPE).

Seiichiro Katsura (Member, IEEE) received the B.E. degree in system design engineering and the M.E. and Ph.D. degrees in integrated design engineering from Keio University, Yokohama, Japan, in 2001, 2002, and 2004, respectively.

From 2003 to 2005, he was a Research Fellow with the Japan Society for the Promotion of Science (JSPS), Tokyo, Japan. From 2005 to 2008, he worked with the Nagaoka University of Technology, Nagaoka, Niigata, Japan. Since 2008, he has been with the Keio University, Yokohama, Japan, where he is currently working as a Professor. In 2017, he was a Visiting Researcher with the Laboratory for Machine Tools and Production Engineering (WZL) of RWTH Aachen University, Aachen, Germany. His current research interests include applied abstraction, human support, data robotics, wave system, systems energy conversion, and electromechanical integration systems.

Prof. Katsura was the recipient of the Institute of Electrical Engineers of Japan (IEEJ) Distinguished Paper Awards, in 2003 and 2017, IEEE Industrial Electronics Society Best Conference Paper Award, in 2012, and JSPS Prize, in 2016. He serves as Associate Editor for the IEEE TRANSACTIONS ON INDUSTRIAL ELECTRONICS, Associate Editor for the IEEE JOURNAL OF EMERGING AND SELECTED TOPICS IN INDUSTRIAL ELECTRONICS, and Technical Editor for IEEE/ASME TRANSACTIONS ON MECHATRONICS.